


Magnetotransport and Berry phase tuning in Gd-doped Bi₂Se₃ topological insulator single crystals

Lei Chen,¹ Shuang-Shuang Li,² Weiyao Zhao^{3,4},,^{3,4} Abdulhakim Bake,^{4,5} David Cortie,^{4,5} Xiaolin Wang,^{4,5} Julie Karel,³ Han Li,^{1,*} and Ren-Kui Zheng^{1,†}

¹*School of Physics and Materials Science, Guangzhou University, Guangzhou 510006, People's Republic of China*

²*School of Materials Science and Engineering and Jiangxi Engineering Laboratory for Advanced Functional Thin Films, Nanchang University, Nanchang 330031, People's Republic of China*

³*Department of Materials Science & Engineering, and ARC Centre of Excellence in Future Low-Energy Electronics Technologies, Monash University, Clayton, Victoria 3800, Australia*

⁴*ISEM, University of Wollongong, North Wollongong, New South Wales 2500, Australia*

⁵*ARC Centre of Excellence in Future Low-Energy Electronics Technologies, University of Wollongong, North Wollongong, New South Wales 2500, Australia*



(Received 4 February 2022; accepted 27 April 2022; published 11 May 2022)

The Berry phase is an important concept in solids, correlated to the band topology, axion electrodynamics, and potential applications of topological materials. Here, we investigate the magnetotransport and Berry phase of rare earth element Gd-doped Bi₂Se₃ (Gd:Bi₂Se₃) topological insulators (TIs) at low temperatures and high magnetic fields. Gd:Bi₂Se₃ single crystals show Shubnikov–de Haas (SdH) oscillations with nontrivial Berry phase, while Bi₂Se₃ single crystals show zero Berry phase in SdH oscillations. A fitting of the temperature-dependent magnetization curves using the Curie-Weiss law reveals that the Gd dopants in the crystals show paramagnetism in the 3–300 K region, indicating that the origin of the Berry phase is not long-range magnetic ordering. Moreover, Gd doping has limited influence on the quantum oscillation parameters (e.g., frequency of oscillation, area of Fermi surface, effective electron mass, and Fermi wave vectors) but has a significant impact on the Hall mobility, carrier density, and band topology. Our results demonstrate that Gd doping can tune the Berry phase of TIs effectively, which may pave the way for the future realization of many predicted exotic transport phenomena of topological origin.

DOI: [10.1103/PhysRevMaterials.6.054202](https://doi.org/10.1103/PhysRevMaterials.6.054202)

I. INTRODUCTION

The Berry phase, an important concept in many fields of physics, was proposed by Berry [1]. It is a geometrical phase of a parallel-transport vector acquired after undergoing a closed trajectory in parameter space. This geometrical phase is only determined by the properties related to closed trajectory in a parameter space. In a crystal, Zak [2] argued that the Berry phase can be obtained on a moving electron in the Brillouin zone (as a parameter space). As a result, the Berry phase of electrons of metals appears in the semiclassical quantization condition for its energy levels (Landau levels), which thus affects the Landau-level-related physical phenomena, e.g., the Shubnikov–de Haas (SdH) oscillation and the de Haas–van Alphen oscillation [3,4]. The nonzero (nontrivial) Berry phase correction to Landau quantization happens on electron orbits that link to band-contact lines, which demonstrates the Bloch band topology in solids [3]. The nontrivial Berry phase has been reported in Dirac semimetals [5–8], Weyl semimetals [9–11], topological nodal-line semimetals [12–18], and other topological materials [19–22]. Since the Berry phase is related

to the band topology, the experimental observation is different in various materials: e.g., $\sim 0.75\pi$ and π in graphite and graphene [23,24], π in Rashba semiconductor BiTeI [25], and $0.25\text{--}0.75\pi$ in Cd₃As₂ [7,8].

The quantum oscillation behaviors are normally observed in metallic materials. However, recent reports broaden this knowledge in various insulating materials with special bulk-band symmetries and metallic surface states, e.g., SmB₆ [26,27], YbB₁₂ [28], Te [29], and (V, Sn):Bi_{1.1}Sb_{0.9}Te₂S [30]. The most discussed materials family is the three-dimensional (3D) topological insulators (TIs), which possess insulating bulk bands and time-reversal-symmetry-protected Dirac surface states, which was theoretically predicted in the Bi₂Se₃ family [31] and experimentally verified [32] in the last decade. The symmetry-protected surface state offers tremendous opportunities for spintronics, non-Abelian quantum computing, and energy-efficient electronic devices. Due to the Dirac band nature of the surface states of 3D TIs, one may obtain the π Berry phase shift on their Landau quantization-related phenomena. However, in practice, the Berry phase situation for a 3D TI can be very complicated; for example, defects shift the bulk Fermi level into the conduction band in Bi₂Se₃ single crystals, resulting in non-Dirac bulk-dominant quantum oscillations with zero Berry phase [33]. Even for surface-dominant transport of 3D TIs, the deviation of the dispersion of the

*lihan@gzhu.edu.cn

†zrk@ustc.edu

surface state from ideal linearity results in a nontrivial Berry phase between zero and π , e.g., 0.44π in $\text{Bi}_2\text{Te}_2\text{Se}$ [34,35].

Another effective way to tune the Berry phase in 3D TIs is magnetic ion doping. Upon doping, the spin texture of the topological surface state changes to a hedgehoglike spin texture; e.g., in a magnetic ion-doped Bi_2Se_3 crystal, the surface state was gapped due to the ferromagnetic ordering, and the spin texture was turned to hedgehog like [36]. The Berry phase in such a magnetic ion-doped TI is defined by the spin texture of the Fermi surface, which in this situation can be tuned from π to zero via shifting the Fermi level to the Dirac point [36,37]. The ferromagnetic state in a TI is very useful, enabling the quantum anomalous Hall effect [38] and paving the way to dissipationless electronic conductance in zero magnetic field. Moreover, tuning the Berry phase to zero in a ferromagnetic TI provides the condition for axion electrodynamics [36,39]. The ferromagnetic ordering has been reported in 3d transition-metal-doped TIs, e.g., $\text{Mn}:\text{Bi}_2\text{Te}_3$ [40,41], $\text{Cr}:\text{TlBiTe}_2$ [42], and $\text{Cr}:\text{Bi}_2\text{Se}_3$ [43]. Recently, rare earth elements have also been considered as magnetic dopants in TI materials, which provide ferromagnetism without significantly harming the high mobility [44,45]. Previous research shows that Gd is a good dopant in 3D TIs; for instance, $\text{Gd}:\text{Bi}_2\text{Te}_3$ shows antiferromagnetism [46], and $\text{Gd}:\text{TlBiTe}_2$ and $\text{Gd}:\text{Bi}_2\text{Se}_3$ show ferromagnetism with large Gd moments ($5\text{--}7\ \mu_B/\text{Gd}$) [47,48]. Therefore, studying the magnetotransport properties of Gd-doped TIs is helpful to understand the Berry phase. Here, we introduce a comprehensive magnetotransport study of $\text{Gd}:\text{Bi}_2\text{Se}_3$ single crystals to illustrate the nontrivial Berry phase in Gd-doped TIs.

II. EXPERIMENTS

A Bridgman method was employed to grow the single crystals of Bi_2Se_3 and $\text{Gd}:\text{Bi}_2\text{Se}_3$. Briefly, high-purity Gd (99.9%), Bi (99.99%), and Se (99.99%) powders ($\sim 10\text{ g}$) in the stoichiometric ratio were mixed and sealed in a quartz tube as starting materials. For the Gd-doped sample, the starting nominal ratio is $\text{Gd}_{0.1}\text{Bi}_{1.9}\text{Se}_3$. The crystal growth was carried out using the following procedure: (i) heating the mixed powders to 1100°C at $1^\circ\text{C}/\text{min}$ to completely melt them; (ii) maintaining at this temperature for 24 h to ensure uniform mixture of Gd, Bi, and Se atoms; and (iii) slowly cooling down to 500°C at $2^\circ\text{C}/\text{h}$ to crystallize the sample; (iv) naturally cooling to room temperature. Since the Gd dopants possess a high melting point, we set the melting temperature at 1100°C in steps (i) and (ii) to ensure full interaction among the molten elements in the liquid state. After the growth process, single-crystal flakes with a typical size of $5\times 5\times 0.2\text{ mm}^3$ can be mechanically exfoliated from the ingot. The single crystals prefer to naturally cleave along the (001) planes, resulting in the c axis being the normal direction of the flakes, as is commonly the case in this family of materials. The dopant distribution of $\text{Gd}:\text{Bi}_2\text{Se}_3$ flakes was confirmed using energy dispersive x-ray spectroscopy (EDS) coupled to a scanning electron microscope. In this paper, we employ the actual Gd, Bi, and Se concentration obtained by EDS as the final composition, which is determined to be $\text{Gd}_{0.02}\text{Bi}_{1.98}\text{Se}_3$.

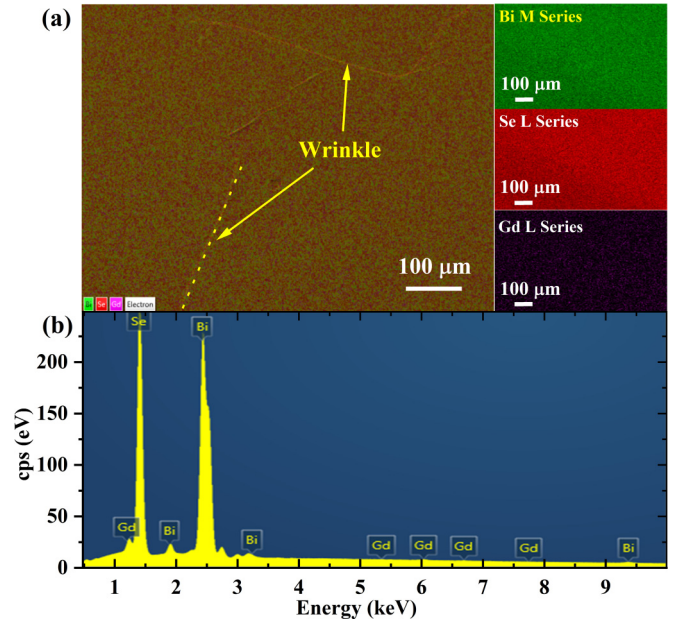


FIG. 1. Scanning electron microscopy (SEM) and EDS characterization of a freshly cleaved $\text{Gd}:\text{Bi}_2\text{Se}_3$ single-crystal surface. (a) The secondary electron image and elemental mapping image are plotted in superposition to illustrate the uniform distribution of all elements. The element mapping of Bi, Se, and Gd in the same area are shown separately on the right side. (b) The EDS of the area scan, in which the peaks are indexed with elements.

The electronic transport properties were measured using a physical properties measurement system (PPMS) (DynaCool-14T, Quantum Design). Hall measurements were performed on a freshly cleaved ab plane of crystals, using room-temperature cured silver paste. The electric current is parallel to the ab plane, while the direction of the magnetic field is perpendicular to the ab plane. The angle dependence of the magnetoresistance (MR) was measured using a horizontal rotational rig mounted on the PPMS. Before rotation, the sample alignment was designed to make sure that the magnetic field was always perpendicular to the electric current. The magnetic measurements were conducted using a vibration sample magnetometer equipped on the PPMS. During temperature-dependent magnetization (MT) measurements, the samples were cooled to 3 K with 500 Oe magnetic field (FC mode) and zero magnetic field (ZFC mode), respectively, after which the magnetization data were collected in the heating process, with applied magnetic field of 500 Oe. Magnetic hysteresis (MH) curves were obtained by scanning the magnetic field between 5 and -5 T at certain temperatures.

III. RESULTS AND DISCUSSION

Before we conducted electronic transport measurements, EDS measurements were performed on the freshly cleaved surface of the crystals to analyze the distribution of Gd dopants. A relatively large area ($500\times 670\ \mu\text{m}^2$) was selected to conduct the measurements to ensure the accuracy of the elemental ratio in the crystal, as shown in Fig. 1(a). The elemental mapping was superimposed to the SEM image to illustrate the elemental distribution with the surface

TABLE I. Elemental concentration of Gd:Bi₂Se₃ single crystals.

Bi ₂ Se ₃ crystals	Bi (atom %)	Se (atom %)	Gd (atom %)
Sample 1	40	59.6	0.4
Sample 2	40.3	59.2	0.4

morphology. There were several wrinkles on the flat surface of the crystal, as demonstrated by the SEM image, which however were not observed in the elemental mapping image. The wrinkles are quite common on the surfaces of a cleaved quasi-two-dimensional (2D) crystal. The SEM backscattered image and elemental mapping results suggest that the Gd dopant is uniformly distributed in the Bi₂Se₃ crystal without segregation. Further, we employ EDS to estimate the Gd-doping level in the as-grown single crystals. Figure 1(b) shows the characteristic peaks of all elements, in which the peak intensities related to the Bi and Se elements are much stronger than that of the Gd element. After analyzing the peak intensity via AZtec software, the elemental concentrations of two different Gd:Bi₂Se₃ samples are summarized in Table I. The selenium vacancies are observed in both samples, which agrees with the literatures [33,49] and is the main reason for the Fermi level shifting into the conduction band. The

Gd-doping levels in both samples are stable at the Gd/Bi ratio ~ 0.01 , which is much lower than the starting Gd/Bi ratio. Since the samples for EDS measurements are typical shiny single-crystal pieces exfoliated from the ingot, we deduce that 1 atom % is a relatively stable doping level for Gd substitution at Bi sites in the aforementioned crystal growth process.

We first revisit the electronic properties of Bi₂Se₃ single crystals grown with the same conditions as that for Gd:Bi₂Se₃ crystals. The Bi₂Se₃ crystals possess a metallic ground state [inset of Fig. 2(a)] due to the Se vacancies. MRs ($MR = [R(B) - R(0)]/R(0)$) in the 3–300 K and 0–14 T region are shown in Fig. 2(a). The total MR at low temperatures, e.g., < 30 K, is $\sim 20\%$ at 14 T, which slightly decreases to $\sim 10\%$ with heating. The linearlike increasing of MR with the magnetic field at low temperatures is also reported in other 3D TIs [30,50]. Another interesting point is that the low-temperature MR vs B curves show obvious oscillation behaviors at high fields, which is due to the Landau quantization, namely, the SdH oscillation. The pure oscillation patterns for $3 \text{ K} \leq T \leq 30 \text{ K}$ can be obtained by subtracting the smooth MR backgrounds and are plotted against $1/B$ in Fig. 2(c). Note that the background-subtracted oscillation patterns at different temperatures show the same phase, however, with decreasing oscillation amplitude upon heating from 3 to

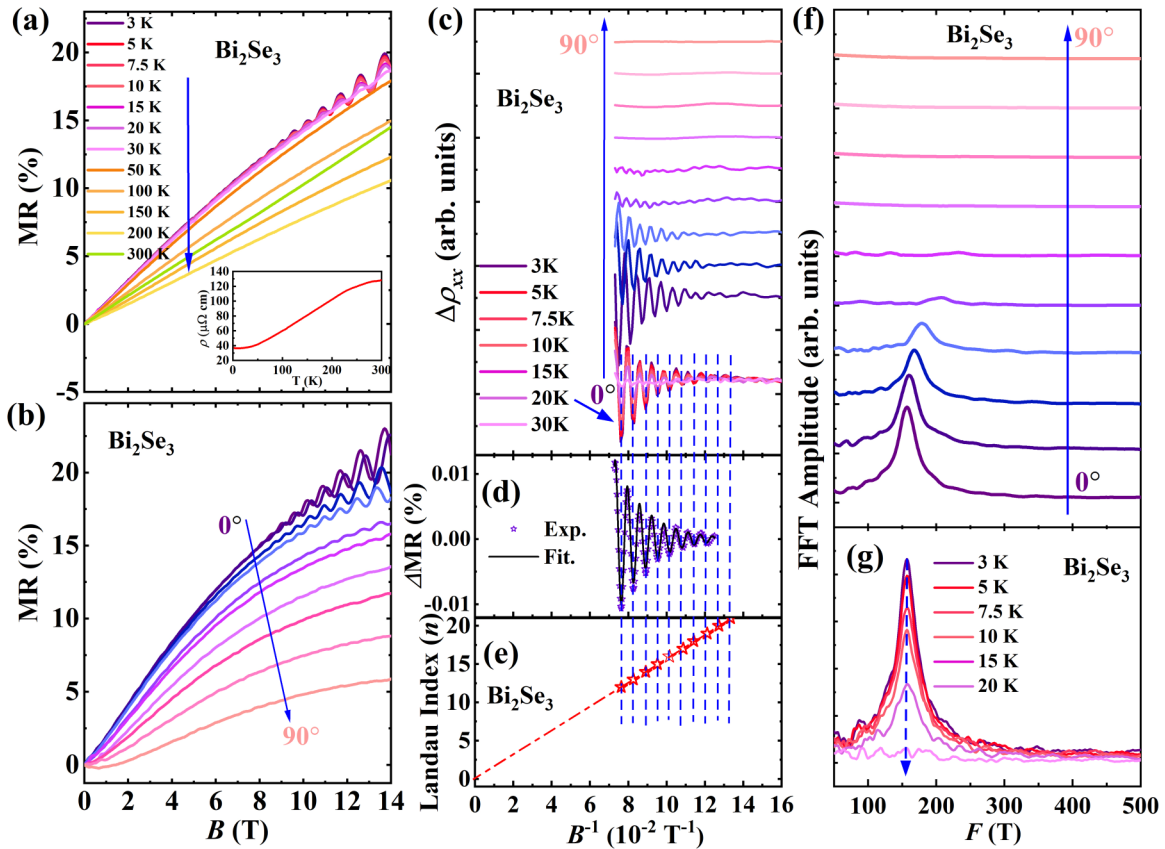


FIG. 2. A glimpse of the magnetotransport properties of a pure Bi₂Se₃ single crystal. (a) and (b) Temperature and angle ($T = 3 \text{ K}$) dependence of the magnetoresistance (MR) vs B curves. (c) Temperature- and angle-dependent oscillation patterns whose amplitude decreases with heating (plotted in superposition of all temperatures, as pointed by the blue arrow) and increasing rotating angle. (d) The Lifshitz-Kosevich (LK) formula fitting of oscillation patterns at $T = 3 \text{ K}$ and $\theta = 0^\circ$. (e) The Landau fan diagram of the oscillation patterns at 0° . (f) and (g) Fast Fourier transform (FFT) amplitude plot during rotating and heating.

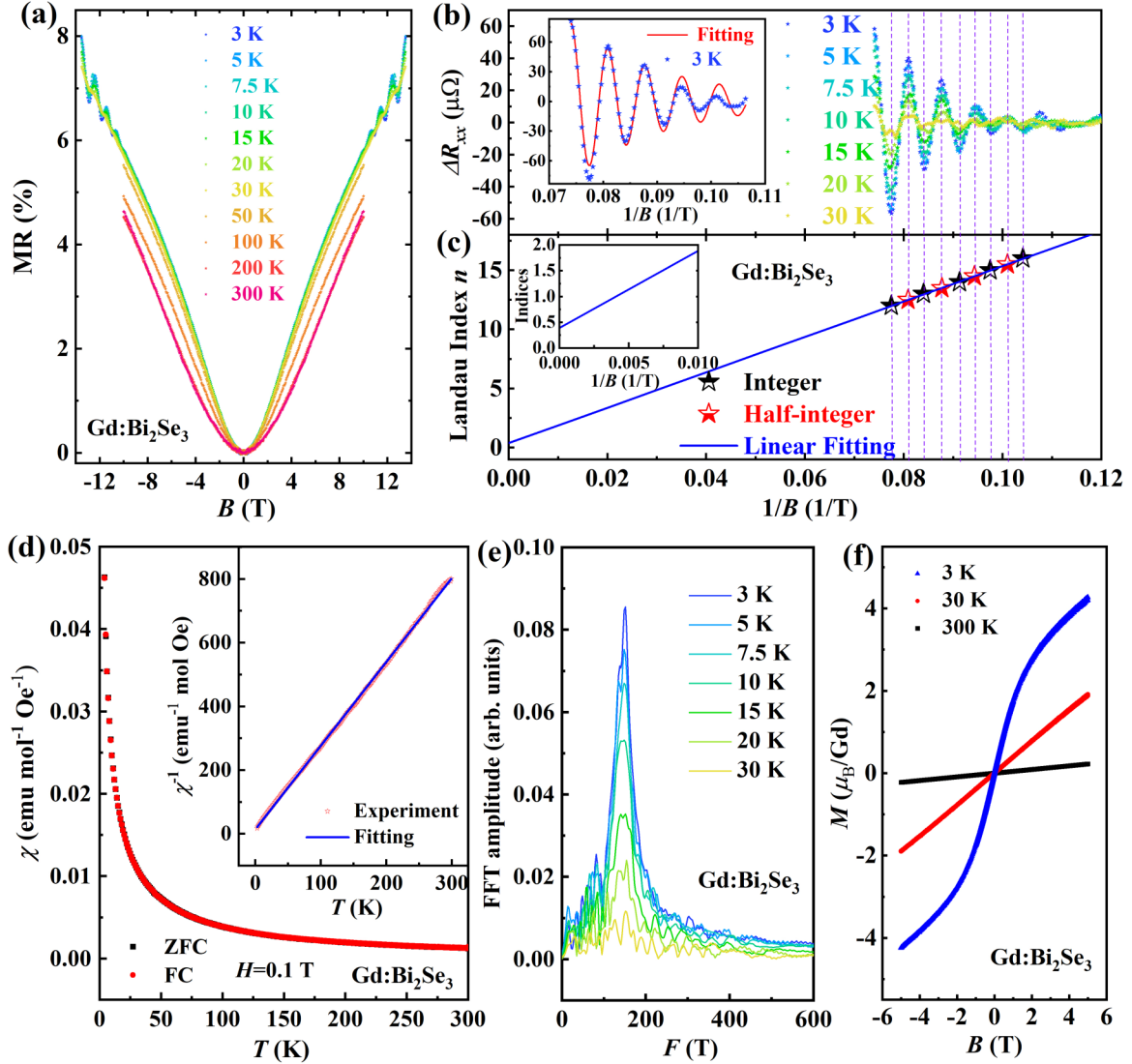


FIG. 3. A glimpse of the magnetotransport and magnetic properties of a Gd:Bi₂Se₃ single crystal. (a) Magnetoresistance (MR) vs B curves at fixed temperatures ranging from 3 to 300 K. (b) The oscillatory patterns of the MR vs $1/B$ curves. Inset: A fitting of the 3-K oscillatory pattern using the Lifshitz-Kosevich (LK) formula. (c) The Landau fan diagram is plotted to illustrate the Berry phase, in which the dot lines guide between the oscillation peaks and dips. (d) Temperature dependence of the zero-field-cooled (ZFC) and field-cooled (FC) magnetic susceptibility. Inset: A fitting of the magnetic data using the Curie-Weiss law. (e) The fast Fourier transform (FFT) spectra of oscillatory patterns. (f) Magnetic hysteresis loops at $T = 3, 30$, and 300 K.

30 K. Therefore, the temperature-dependent SdH oscillation patterns are plotted in superposition [lower panel of Fig. 2(c)]. Since the Bi₂Se₃ crystals show metallic ground states, the SdH oscillations can be described by the Lifshitz-Kosevich (LK) formula, with the Berry phase being considered:

$$\frac{\Delta\rho}{\rho(0)} = \frac{5}{2} \left(\frac{B}{2F} \right)^{1/2} R_T R_D R_S \cos \left[2\pi \left(\frac{F}{B} + \gamma - \delta \right) \right],$$

where $R_T = \alpha T m^* / B \sinh(\alpha T m^* / B)$, $R_D = \exp(-\alpha T_D m^* / B)$, and $R_S = \cos(\alpha g m^* / 2)$. Here, m^* is the ratio of effective cyclotron mass to the free electron mass m_e ; g is the g factor; T_D is the Dingle temperature; and $\alpha = (2\pi^2 k_B m_e) / \hbar e$, where k_B is the Boltzmann constant, \hbar is the reduced Planck constant, and e is the elementary charge. The oscillation of $\Delta\rho$ is described by the cosine term with a phase factor $\gamma - \delta$, in

which $\delta = 0$ for 2D Fermi pockets, and $\pm \frac{1}{8}$ for 3D Fermi pockets, $\gamma = \frac{1}{2} - \Phi_B / 2\pi$, where Φ_B is the Berry phase. The Landau quantization modulates the conductivity (σ_{xx}) in magnetic fields, which shows a peak with the Fermi level locating on Landau levels. In the Bi₂Se₃ system, the Berry phase of SdH oscillations can also be obtained by extrapolating the Landau level index n to the extreme field limit ($1/B \rightarrow 0$) in the Landau fan diagram, as shown in Fig. 2(e). Our resistivity measurements show that $\rho_{xx} \ll \rho_{xy}$ for Bi₂Se₃ crystals, which means that σ_{xx} is in phase with ρ_{xx} . We assign the maximum of the oscillations as the half-integer Landau index, the minimum of the oscillations as the integer Landau index, respectively, and linearly fitted the data [51,52]. In this case, the $\frac{1}{2}$ phase shift in γ has been considered in the Landau indices assignment, which means that, with a trivial

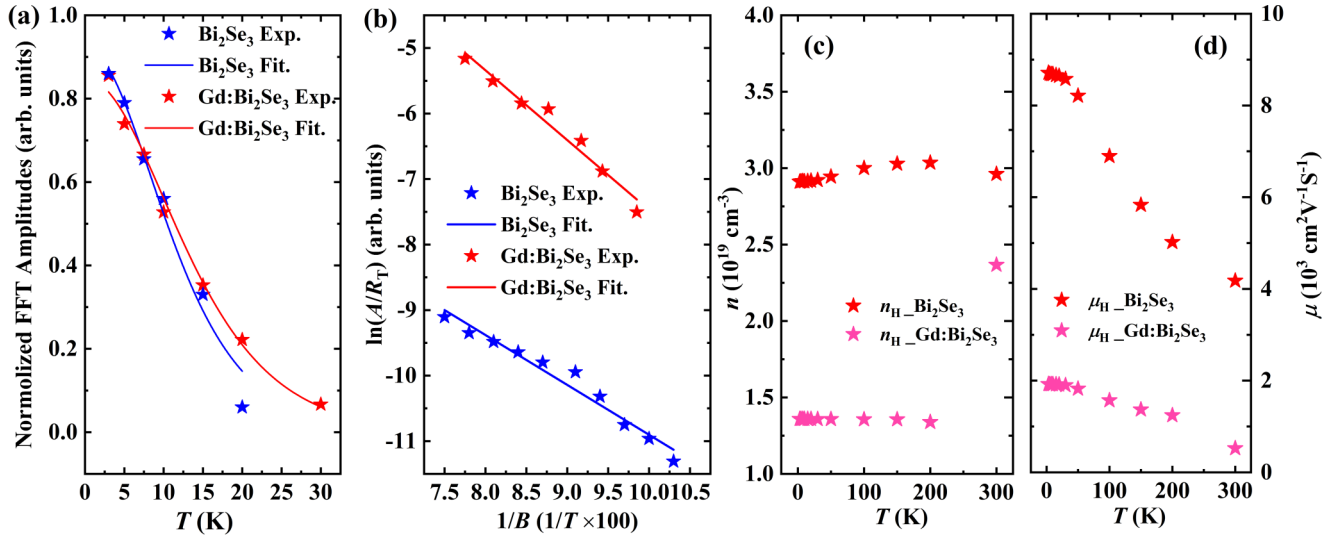


FIG. 4. The carrier's properties of Bi₂Se₃ and Gd:Bi₂Se₃ single crystals. (a) The Lifshitz-Kosevich (LK) formula fitting to obtain the effective mass of electrons. (b) The Dingle plots. Temperature dependence of the (c) carrier density and (d) mobility obtained from Hall measurements.

Berry phase, the intercept is 0. The oscillation patterns can be fitted with the LK formula, as shown in Fig. 2(d), from which the obtained Berry phase is $0.05 \pm 0.02\pi$. As shown in Fig. 2(e), the intercept of the straight line with the y axis is zero, which agrees with the fitting in Fig. 2(d), meaning that the Fermi pockets contributing to SdH oscillations in the Bi₂Se₃ single crystal are topologically trivial bulk bands. Further, the angular dependence of SdH oscillation measurements was conducted to analyze the morphology of the related Fermi pocket, as shown in Fig. 2(b). After subtracting the smooth MR backgrounds, the oscillation patterns are shown in Fig. 2(c). The corresponding fast Fourier transform (FFT) results are shown in Fig. 2(f). The oscillations show 2D-like behaviors, which is probably contributed by some 2D-like trivial bands. Therefore, we deduce that the Fermi level is sitting on the edge of the bulk conduction band, where the near-edge 2D electron gas (2DEG) contributes mainly to the quantum oscillations [53–56]. The rest of the information obtained from the Bi₂Se₃ crystals together with the SdH of Gd:Bi₂Se₃ crystals will be discussed later.

Similarly, a freshly cleaved Gd:Bi₂Se₃ single crystal is employed to conduct MR measurements at various fixed temperatures, with applied external magnetic fields up to 14 T, as shown in Fig. 3(a). The quasilinear MR with the magnetic field is like the observation in Bi₂Se₃ crystals, and the maximum MR values (e.g., MR at 14 T is $\sim 8\% < 50$ K) decrease slightly with heating from 3 K. Another similarity is the low-temperature oscillation patterns, which can be

obtained by subtracting smooth MR backgrounds, as shown in Fig. 3(b). The SdH oscillation patterns are in phase with each other at different temperatures; however, the oscillation amplitudes decrease with heating, as described by the thermal damping factor in the LK formula. Let us pay attention to the Berry phase in the Gd:Bi₂Se₃ crystal obtained from the Landau fan diagram shown in Fig. 3(c). During linear fitting, we employ the same assigning rule as that for the Bi₂Se₃ crystals since $\rho_{xx} \ll \rho_{xy}$ also manifests here. The intercept of the straight line with the y axis is 0.4, as shown in the zoom-in plot at the high field limit [inset of Fig. 3(c)]. Therefore, a nonzero Berry phase of 0.8π is obtained with 1 atom% Gd doping in Bi₂Se₃. To further illustrate this point, we employ the LK formula to fit the oscillation pattern at 3 K, as shown in the inset of Fig. 3(b). A Berry phase of $0.78 \pm 0.04\pi$ is obtained from the fitting, which agrees well with that obtained from the Landau fan diagram. Further, we conducted magnetic measurements on the Gd:Bi₂Se₃ crystal to search for possible magnetic ordering which may contribute to the Berry phase. As shown in Fig. 3(d), the ZFC and FC MT curves coincide with each other perfectly, and there is no obvious magnetic transition. The magnetism of trivalent lanthanide group ions originates from unpaired electrons, which can be described by the Curie law $\chi = C/T$ and Curie-Weiss law $\chi = C/(T + \theta_p)$. Here, C is the Curie constant, and the Weiss constant θ_p typically accounts for the magnetic ordering of the electronic moments below the Curie or Néel temperature for uncorrelated spins. The fitting

TABLE II. The quantum oscillation and carrier parameters at $T = 3$ K: SdH frequency F , cross-sectional Fermi surface area A_F , Fermi vector k_F , effective electron mass m^* , Fermi velocity v_F , quantum mobility μ_Q , carrier density (n_{H-3K}) and mobility (μ_{H-3K}) from Hall measurements, and the Berry phase Φ_B .

	F (T)	A_F (Å ⁻²)	k_F (Å ⁻¹)	m^* (m_e)	v_F (m/s)	μ_Q (cm ² /Vs)	n_{H-3K} (cm ⁻³)	μ_{H-3K} (cm ² /Vs)	Φ_B
Bi ₂ Se ₃	157	0.15	0.22	0.2	2.2×10^5	310	2.8×10^{19}	8400	0
Gd : Bi ₂ Se ₃	151	0.14	0.21	0.16	2.8×10^5	637	1.38×10^{19}	1500	0.8π

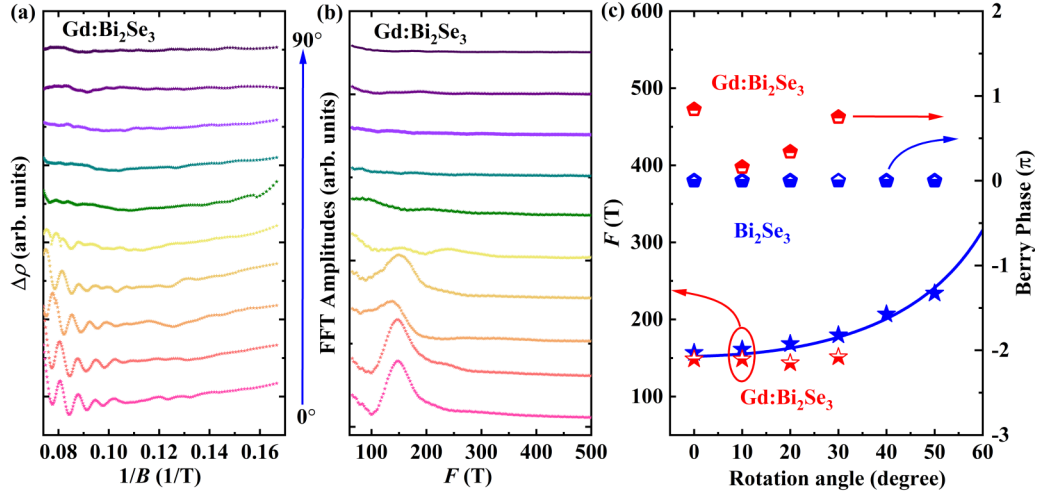


FIG. 5. Angular-dependent Shubnikov-de Haas (SdH) oscillations of Gd:Bi₂Se₃ single crystals. (a) The SdH oscillation patterns obtained from the angular dependent magnetoresistance (MR) curves from which smooth backgrounds have been subtracted. (b) Fast Fourier transform (FFT) spectra of the oscillation patterns in (a). (c) The SdH oscillation frequencies and Berry phase are plotted as a function of the rotation angle. Note that the blue line is the cosine fitting of the Bi₂Se₃ SdH oscillation frequency, which indicates the frequency change of an ideal two-dimensional (2D) Fermi surface.

of the Curie-Weiss law is shown in the inset of Fig. 3(d). The obtained Curie constant C is $\sim 2.5 \text{ emu K mol}^{-1} \text{ Oe}^{-1}$, and θ_p is $\sim 0.4 \text{ K}$, which are neglectable. Here, $C = (N_A \mu_{\text{eff}}^2)/3k_B$, where N_A is the Avogadro number, k_B is the Boltzmann constant; therefore, the effective momentum μ_{eff} of Gd is $\sim 4.5 \mu_B$. The MH curves at 3, 30, and 300 K also show paramagnetic behaviors, as shown in Fig. 3(f). Therefore, the Gd dopants in the crystals show paramagnetism, indicating that the origin of the Berry phase is not the long-range magnetic ordering.

Further, one may learn the fermiology from the SdH oscillations using the LK formula, e.g., the area of the Fermi pockets, the Fermi vector, the Fermi velocity, and the cyclotron mass of electron. According to the Onsager-Lifshitz equation, the frequency of quantum oscillations $F = (\varphi_0/2\pi^2)A_F$, where A_F is the extremal cross-sectional area of the Fermi surface perpendicular to the magnetic field, and φ_0 is the magnetic flux quantum. The quantum oscillation frequencies of Bi₂Se₃ and Gd:Bi₂Se₃ from the FFT results in Figs. 2(g) and 3(e) are 157 and 151 T, respectively. Therefore, the cross-section areas A_F related to the Fermi pockets in Bi₂Se₃ and Gd:Bi₂Se₃ are 0.15 and 0.144 Å², respectively. Using $A_F = \pi k_F^2$, the Fermi wave vectors k_F are 0.22 and 0.21 Å⁻¹ for Bi₂Se₃ and Gd:Bi₂Se₃, respectively. According to the LK formula, the effective mass of carriers contributing to the SdH effect can be obtained through fitting the temperature dependence of the oscillation amplitude to the thermal damping factor R_T , which is shown in Fig. 4(a). During the fitting, we employ the normalized FFT amplitudes at various temperatures. The effective masses obtained from R_T fitting are $0.20 \pm 0.01 m_e$ for Bi₂Se₃ and $0.16 \pm 0.01 m_e$ for Gd:Bi₂Se₃, which are like the obtained values from transport and angle-resolved photoemission spectroscopy measurements, e.g., 0.12–0.24 m_e [44,57,58]. Thus, one can obtain the Fermi velocities $v_F = \hbar k_F/m^* \sim 2.2 \times 10^5 \text{ m/s}$ for Bi₂Se₃ and $2.8 \times 10^5 \text{ m/s}$ for Gd:Bi₂Se₃. From the field damping relationship, we fit the Dingle tem-

peratures via the Dingle plot, as shown in Fig. 4(b), for both samples, which are 32 and 21 K for Bi₂Se₃ and Gd:Bi₂Se₃, respectively. The quantum relaxation time and quantum mobility can also be obtained by $\tau = \hbar/2\pi k_B T_D$ (3.8 and 5.8 fs for Bi₂Se₃ and Gd:Bi₂Se₃) and $\mu_Q = e\tau/m^*$ (310 and 637 cm²/Vs for Bi₂Se₃ and Gd:Bi₂Se₃), respectively. The parameters of the carrier calculated from the quantum oscillations are summarized in Table II together with density and mobility of the carrier. Hall measurements are also conducted on Bi₂Se₃ and Gd:Bi₂Se₃ single crystals from 3 to 300 K, from which the properties of the carrier are calculated and plotted in Figs. 4(c) and 4(d). Further, we conduct angular-dependent SdH measurements on a Gd:Bi₂Se₃ single crystal at 3 K, as shown in Fig. 5(a). The quantum oscillation patterns are clear in the low-angle area, which is like those for Bi₂Se₃ [Fig. 2(c)]. The oscillation frequencies can be obtained via FFT spectra, as shown in Fig. 5(b). Interestingly, the frequency seems not to be shifting obviously during the rotation of the crystal, which is different from the 2D-like behavior in Bi₂Se₃. Therefore, we plot the FFT frequencies of Bi₂Se₃ and Gd:Bi₂Se₃ against the rotation angle in Fig. 5(c). Note that, for a 2D Fermi surface, the angular-dependent SdH frequency $F(\theta)$ increases in an inverse cosine rule: $F(\theta) = F(0)/\cos(\theta)$, which is shown as a fitting line in Fig. 5(c). As expected, the Bi₂Se₃ follows the 2D rotation rule during rotation. However, the SdH frequencies of Gd:Bi₂Se₃ are roughly constant during rotation, which indicates that the related Fermi pocket is not contributed by 2DEG. Further, we employ the Landau fan diagram to analyze the Berry phase shifting at different rotation angles, which are also shown in Fig. 5(c). The Berry phase for Bi₂Se₃ is always zero since its oscillations are contributed by 2DEG. However, for Gd:Bi₂Se₃, the Berry phase keeps changing during rotation, regardless of the nearly constant frequency. Therefore, Gd doping has a limited influence on the morphology of the Fermi surface but contributes to the band topology significantly.

IV. CONCLUSIONS

We employed a modified Bridgeman method to grow Gd-doped Bi_2Se_3 single-crystal TIs. The Gd dopant distributes uniformly in the crystals, in which the doping level is ~ 1 atom % in Bi sites, as verified by EDS. The magnetic measurements show that no long-range magnetic ordering forms in Gd: Bi_2Se_3 crystals > 3 K, ruling out the possible magnetic ordering-induced Berry phase. Magnetotransport measurements on Gd: Bi_2Se_3 single crystals show that Gd doping has minor effects on SdH oscillation frequency, Fermi surface area, Fermi wave vectors, and effective electron mass of Bi_2Se_3 crystals. However, Gd doping reduces the Hall mobility and carrier density and modifies the Berry phase and band topology of Bi_2Se_3 , namely, the major contribution of the Fermi pocket changes from the 2D-like electron gas state with

trivial topology and zero Berry phase to the topological surface state with nontrivial topology and 0.8π Berry phase. The engineering of the Berry phase by Gd doping may provide more possibilities for the application of TIs in electronic/spintronic devices.

ACKNOWLEDGMENTS

This paper is supported by the National Natural Science Foundation of China (Grant No. 11974155). W.Z., A.B., D.C., X.W., and J.K. acknowledge the support from ARC Centre of Excellence in Future Low-Energy Electronics Technologies No. CE170100039. J.K. and W.Z. acknowledge Australian Research Council Discovery Project No. DP200102477.

-
- [1] M. V. Berry, Quantal phase factors accompanying adiabatic changes, *Proc. R. Soc. Lond.* **392**, 45 (1984).
 - [2] J. Zak, Berry's Phase for Energy Bands in Solids, *Phys. Rev. Lett.* **62**, 2747 (1989).
 - [3] G. Mikitik and Y. V. Sharlai, Manifestation of Berry's Phase in Metal Physics, *Phys. Rev. Lett.* **82**, 2147 (1999).
 - [4] D. Shoenberg, *Magnetic Oscillations in Metals* (Cambridge University Press, Cambridge, 2009).
 - [5] X. Yuan, C. Zhang, Y. Liu, A. Narayan, C. Song, S. Shen, X. Sui, J. Xu, H. Yu, Z. An, J. Zhao, S. Sanvito, H. Yan, and F. Xiu, Observation of quasi-two-dimensional Dirac fermions in ZrTe_5 , *NPG Asia Mater.* **8**, e325 (2016).
 - [6] J. B. He, Y. Fu, L. X. Zhao, H. Liang, D. Chen, Y. M. Leng, X. M. Wang, J. Li, S. Zhang, M. Q. Xue, C. H. Li, P. Zhang, Z. A. Ren, and G. F. Chen, Quasi-two-dimensional massless Dirac fermions in CaMnSb_2 , *Phys. Rev. B* **95**, 045128 (2017).
 - [7] L. P. He, X. C. Hong, J. K. Dong, J. Pan, Z. Zhang, J. Zhang, and S. Y. Li, Quantum Transport Evidence for the Three-Dimensional Dirac Semimetal Phase in Cd_3As_2 , *Phys. Rev. Lett.* **113**, 246402 (2014).
 - [8] A. Narayanan, M. D. Watson, S. F. Blake, N. Bruyant, L. Drigo, Y. L. Chen, D. Prabhakaran, B. Yan, C. Felser, T. Kong, P. C. Canfield, and A. I. Coldea, Linear Magnetoresistance Caused by Mobility Fluctuations in N-Doped Cd_3As_2 , *Phys. Rev. Lett.* **114**, 117201 (2015).
 - [9] X. Huang, L. Zhao, Y. Long, P. Wang, D. Chen, Z. Yang, H. Liang, M. Xue, H. Weng, Z. Fang, X. Dai, and G. Chen, Observation of the Chiral-Anomaly-Induced Negative Magnetoresistance in 3D Weyl Semimetal TaAs, *Phys. Rev. X* **5**, 031023 (2015).
 - [10] J. Hu, J. Y. Liu, D. Graf, S. M. A. Radmanesh, D. J. Adams, A. Chuang, Y. Wang, I. Chiorescu, J. Wei, L. Spinu, and Z. Q. Mao, π Berry phase and Zeeman splitting of Weyl semimetal TaP, *Sci. Rep.* **6**, 18674 (2016).
 - [11] P. Sergelius, J. Gooth, S. Baessler, R. Zierold, C. Wiegand, A. Niemann, H. Reith, C. Shekhar, C. Felser, B. Yan, and K. Nielsch, Berry phase and band structure analysis of the Weyl semimetal NbP, *Sci. Rep.* **6**, 33859 (2016).
 - [12] M. Matusiak, J. R. Cooper, and D. Kaczorowski, Thermoelectric quantum oscillations in ZrSiS , *Nat. Commun.* **8**, 15219 (2017).
 - [13] Q. Chen, Z. Lou, S. Zhang, B. Xu, Y. Zhou, H. Chen, S. Chen, J. Du, H. Wang, J. Yang, Q. Wu, O. V. Yazyev, and M. Fang, Large magnetoresistance and non-zero Berry phase in the nodal-line semimetal MoO_2 , *Phys. Rev. B* **102**, 165133 (2020).
 - [14] J. Liu, P. Liu, K. Gordon, E. Emmanouilidou, J. Xing, D. Graf, B. C. Chakoumakos, Y. Wu, H. Cao, D. Dessau, Q. Liu, and N. Ni, Nontrivial topology in the layered Dirac nodal-line semimetal candidate SrZnSb_2 with distorted Sb square nets, *Phys. Rev. B* **100**, 195123 (2019).
 - [15] Y. Yang, H. Xing, G. Tang, C. Hua, C. Yao, X. Yan, Y. Lu, J. Hu, Z. Mao, and Y. Liu, Anisotropic Berry phase in the Dirac nodal-line semimetal ZrSiS : The effect of spin-orbit coupling, *Phys. Rev. B* **103**, 125160 (2021).
 - [16] R. Singha, A. K. Pariari, B. Satpati, and P. Mandal, Large non-saturating magnetoresistance and signature of nondegenerate Dirac nodes in ZrSiS , *Proc. Natl. Acad. Sci. USA* **114**, 2468 (2017).
 - [17] S. Li, Z. Guo, D. Fu, X. C. Pan, J. Wang, K. Ran, S. Bao, Z. Ma, Z. Cai, R. Wang, R. Yu, J. Sun, F. Song, and J. Wen, Evidence for a Dirac nodal-line semimetal in SrAs_3 , *Sci. Bull.* **63**, 535 (2018).
 - [18] L. Guo, T. W. Chen, C. Chen, L. Chen, Y. Zhang, G. Y. Gao, J. Yang, X. G. Li, W. Y. Zhao, and S. Dong, Electronic transport evidence for topological nodal-line semimetals of ZrGeSe single crystals, *ACS Appl. Electron.* **1**, 869 (2019).
 - [19] S. Xu, L. Zhou, H. Wang, X. Y. Wang, Y. Su, P. Cheng, H. Weng, and T. L. Xia, Quantum oscillations and electronic structure in the large-Chern number semimetal RhSn , *Phys. Rev. B* **100**, 245146 (2019).
 - [20] L. Ye, M. K. Chan, R. D. McDonald, D. Graf, M. Kang, J. Liu, T. Suzuki, R. Comin, L. Fu, and J. G. Checkelsky, de Haas-van Alphen effect of correlated Dirac states in kagome metal Fe_3Sn_2 , *Nat. Commun.* **10**, 4870 (2019).
 - [21] Y. Fang, F. Tang, Y. R. Ruan, J. M. Zhang, H. Zhang, H. Gu, W. Y. Zhao, Z. D. Han, W. Tian, B. Qian, X. F. Jiang, X. M. Zhang, and X. Ke, Magnetic-field-induced nontrivial electronic state in

- the Kondo-lattice semimetal CeSb, *Phys. Rev. B* **101**, 094424 (2020).
- [22] K. A. M. H. Siddiquee, R. Munir, C. Dissanayake, X. Hu, S. Yadav, Y. Takano, E. S. Choi, D. Le, T. S. Rahman, and Y. Nakajima, Fermi surfaces of the topological semimetal CaSn_3 probed through de Haas van Alphen oscillations, *J. Phys.: Condens. Matter* **33**, 17LT01 (2021).
- [23] I. A. Luk'yanchuk and Y. Kopelevich, Phase Analysis of Quantum Oscillations in Graphite, *Phys. Rev. Lett.* **93**, 166402 (2004).
- [24] Y. B. Zhang, Y. W. Tan, H. L. Stormer, and P. Kim, Experimental observation of the quantum Hall effect and Berry's phase in graphene, *Nature (London)* **438**, 201 (2005).
- [25] H. Murakawa, M. S. Bahramy, M. Tokunaga, Y. Kohama, C. Bell, Y. Kaneko, N. Nagaosa, H. Y. Hwang, and Y. Tokura, Detection of Berry's phase in a bulk Rashba semiconductor, *Science* **342**, 1490 (2013).
- [26] O. Erten, P. Ghaemi, and P. Coleman, Kondo Breakdown and Quantum Oscillations in SmB_6 , *Phys. Rev. Lett.* **116**, 046403 (2016).
- [27] G. Li, Z. Xiang, F. Yu, T. Asaba, B. Lawson, P. Cai, C. Tinsman, A. Berkley, S. Wolgast, and Y. S. Eo, Two-dimensional Fermi surfaces in Kondo insulator SmB_6 , *Science* **346**, 1208 (2014).
- [28] Z. Xiang, Y. Kasahara, T. Asaba, B. Lawson, C. Tinsman, L. Chen, K. Sugimoto, S. Kawaguchi, Y. Sato, and G. Li, Quantum oscillations of electrical resistivity in an insulator, *Science* **362**, 65 (2018).
- [29] N. Zhang, G. Zhao, L. Li, P. Wang, L. Xie, B. Cheng, H. Li, Z. Lin, C. Xi, and J. Ke, Magnetotransport signatures of Weyl physics and discrete scale invariance in the elemental semiconductor tellurium, *Proc. Natl. Acad. Sci. USA* **117**, 11337 (2020).
- [30] W. Zhao, L. Chen, Z. Yue, Z. Li, D. Cortie, M. Fuhrer, and X. Wang, Quantum oscillations of robust topological surface states up to 50 K in thick bulk-insulating topological insulator, *npj Quantum Mater.* **4**, 56 (2019).
- [31] H. Zhang, C. X. Liu, X. L. Qi, X. Dai, Z. Fang, and S. C. Zhang, Topological insulators in Bi_2Se_3 , Bi_2Te_3 and Sb_2Te_3 with a single Dirac cone on the surface, *Nat. Phys.* **5**, 438 (2009).
- [32] Y. Chen, J. G. Analytis, J. H. Chu, Z. Liu, S. K. Mo, X. L. Qi, H. Zhang, D. Lu, X. Dai, and Z. Fang, Experimental realization of a three-dimensional topological insulator Bi_2Te_3 , *Science* **325**, 178 (2009).
- [33] M. Busch, O. Chiatti, S. Pezzini, S. Wiedmann, J. Sánchez-Barriga, O. Rader, L. V. Yashina, and S. F. Fischer, High-temperature quantum oscillations of the Hall resistance in bulk Bi_2Se_3 , *Sci. Rep.* **8**, 485 (2018).
- [34] A. Taskin and Y. Ando, Berry phase of nonideal Dirac fermions in topological insulators, *Phys. Rev. B* **84**, 035301 (2011).
- [35] Z. Ren, A. Taskin, S. Sasaki, K. Segawa, and Y. Ando, Large bulk resistivity and surface quantum oscillations in the topological insulator $\text{Bi}_2\text{Te}_2\text{Se}$, *Phys. Rev. B* **82**, 241306(R) (2010).
- [36] S. Y. Xu, M. Neupane, C. Liu, D. Zhang, A. Richardella, L. A. Wray, N. Alidoust, M. Leandersson, T. Balasubramanian, and J. Sánchez-Barriga, Hedgehog spin texture and Berry's phase tuning in a magnetic topological insulator, *Nat. Phys.* **8**, 616 (2012).
- [37] H. Z. Lu, J. Shi, and S. Q. Shen, Competition between Weak Localization and Antilocalization in Topological Surface States, *Phys. Rev. Lett.* **107**, 076801 (2011).
- [38] C. Z. Chang, J. Zhang, X. Feng, J. Shen, Z. Zhang, M. Guo, K. Li, Y. Ou, P. Wei, and L. L. Wang, Experimental observation of the quantum anomalous Hall effect in a magnetic topological insulator, *Science* **340**, 167 (2013).
- [39] A. M. Essin, J. E. Moore, and D. Vanderbilt, Magnetoelectric Polarizability and Axion Electrodynamics in Crystalline Insulators, *Phys. Rev. Lett.* **102**, 146805 (2009).
- [40] Y. Hor, P. Roushan, H. Beidenkopf, J. Seo, D. Qu, J. Checkelsky, L. Wray, D. Hsieh, Y. Xia, and S. Y. Xu, Development of ferromagnetism in the doped topological insulator $\text{Bi}_{2-x}\text{Mn}_x\text{Te}_3$, *Phys. Rev. B* **81**, 195203 (2010).
- [41] J. G. Checkelsky, J. Ye, Y. Onose, Y. Iwasa, and Y. Tokura, Dirac-fermion-mediated ferromagnetism in a topological insulator, *Nat. Phys.* **8**, 729 (2012).
- [42] Z. Wang, K. Segawa, S. Sasaki, A. Taskin, and Y. Ando, Ferromagnetism in Cr-doped topological insulator TlSbTe_2 , *APL Mater.* **3**, 083302 (2015).
- [43] P. Haazen, J. B. Laloë, T. Nummy, H. Swagten, P. Jarillo-Herrero, D. Heiman, and J. Moodera, Ferromagnetism in thin-film Cr-doped topological insulator Bi_2Se_3 , *Appl. Phys. Lett.* **100**, 082404 (2012).
- [44] W. Zhao, C. X. Trang, Q. Li, L. Chen, Z. Yue, A. Bake, C. Tan, L. Wang, M. Nancarrow, and M. Edmonds, Massive Dirac fermions and strong Shubnikov-de Haas oscillations in single crystals of the topological insulator Bi_2Se_3 doped with Sm and Fe, *Phys. Rev. B* **104**, 085153 (2021).
- [45] T. Chen, W. Liu, F. Zheng, M. Gao, X. Pan, G. Van Der Laan, X. Wang, Q. Zhang, F. Song, and B. Wang, High-mobility Sm-doped Bi_2Se_3 ferromagnetic topological insulators and robust exchange coupling, *Adv. Mater.* **27**, 4823 (2015).
- [46] J. Kim, K. Lee, T. Takabatake, H. Kim, M. Kim, and M. H. Jung, Magnetic transition to antiferromagnetic phase in gadolinium substituted topological insulator Bi_2Te_3 , *Sci. Rep.* **5**, 10309 (2015).
- [47] S. Filnov, I. I. Klimovskikh, D. Estyunin, A. Fedorov, V. Y. Voroshnin, A. Koroleva, A. G. Rybkin, E. Shevchenko, Z. S. Aliev, and M. Babanly, Probe-dependent Dirac-point gap in the gadolinium-doped thallium-based topological insulator $\text{TlBi}_{0.9}\text{Gd}_{0.1}\text{Se}_2$, *Phys. Rev. B* **102**, 085149 (2020).
- [48] Y. Song, F. Yang, M. Y. Yao, F. Zhu, L. Miao, J. P. Xu, M. X. Wang, H. Li, X. Yao, and F. Ji, Large magnetic moment of gadolinium substituted topological insulator: $\text{Bi}_{1.98}\text{Gd}_{0.02}\text{Se}_3$, *Appl. Phys. Lett.* **100**, 242403 (2012).
- [49] A. Tayal, D. Kumar, and A. Lakhani, Role of lattice inhomogeneities on the electronic properties of selenium deficient Bi_2Se_3 , *J. Phys.: Condens. Matter* **29**, 445704 (2017).
- [50] M. Novak, S. Sasaki, K. Segawa, and Y. Ando, Large linear magnetoresistance in the Dirac semimetal TlBiSSe , *Phys. Rev. B* **91**, 041203(R) (2015).
- [51] W. Zhao, D. Cortie, L. Chen, Z. Li, Z. Yue, and X. Wang, Quantum oscillations in iron-doped single crystals of the topological insulator Sb_2Te_3 , *Phys. Rev. B* **99**, 165133 (2019).
- [52] F. X. Xiang, X. L. Wang, M. Veldhorst, S. X. Dou, and M. S. Fuhrer, Observation of topological transition of Fermi surface from a spindle torus to a torus in bulk Rashba spin-split BiTeCl , *Phys. Rev. B* **92**, 035123 (2015).
- [53] P. King, R. C. Hatch, M. Bianchi, R. Ovsyannikov, C. Lupulescu, G. Landolt, B. Slomski, J. Dil, D. Guan, and J. Mi, Large Tunable Rashba Spin Splitting of a Two-Dimensional Electron Gas in Bi_2Se_3 , *Phys. Rev. Lett.* **107**, 096802 (2011).

- [54] M. Bianchi, R. C. Hatch, J. Mi, B. B. Iversen, and P. Hofmann, Simultaneous Quantization of Bulk Conduction and Valence States Through Adsorption of Nonmagnetic Impurities on Bi_2Se_3 , *Phys. Rev. Lett.* **107**, 086802 (2011).
- [55] H. M. Benia, C. Lin, K. Kern, and C. R. Ast, Reactive Chemical Doping of the Bi_2Se_3 Topological Insulator, *Phys. Rev. Lett.* **107**, 177602 (2011).
- [56] M. Bianchi, D. Guan, S. Bao, J. Mi, B. B. Iversen, P. D. King, and P. Hofmann, Coexistence of the topological state and a two-dimensional electron gas on the surface of Bi_2Se_3 , *Nat. Commun.* **1**, 128 (2010).
- [57] K. Eto, Z. Ren, A. A. Taskin, K. Segawa, and Y. Ando, Angular-dependent oscillations of the magnetoresistance in Bi_2Se_3 due to the three-dimensional bulk Fermi surface, *Phys. Rev. B* **81**, 195309 (2010).
- [58] J. G. Analytis, R. D. McDonald, S. C. Riggs, J. -H. Chu, G. S. Boebinger, and I. R. Fisher, Two-dimensional surface state in the quantum limit of a topological insulator, *Nat. Phys.* **6**, 960 (2010).